Two-dimensional quantum droplets and vortices in Rydberg-dressed Bose gases

Yu-Peng Feng (冯宇鹏)[1], Lin-Xue Wang (王林雪)[1], Bin Liu (刘彬)[2], Yong-Yao Li (黎永耀)[2], and Xiao-Fei Zhang (张晓斐)*[1]

[1]School of Physics and Information Science, Shaanxi University of Science and Technology, Xi'an 710021, China

[2]School of Physics and Optoelectronic Engineering, Foshan University, Foshan 528000, China

October 20, 2026

Abstract

We systematically explore isotropic self-bound liquid states and topological vortex excitations in two-dimensional binary Bose-Einstein condensates with tunable Rydberg soft-core interactions, modeled by the Gross-Pitaevskii equation incorporating the two-dimensional Lee-Huang-Yang quantum correction. Combining analytical Thomas-Fermi treatment with high-precision numerical simulations, we obtain stable fundamental and vortex-carrying quantum droplet solutions and investigate their collisional dynamics. The particle number N and Rydberg coupling strength κ are shown to systematically modulate the spatial and thermodynamic properties of both vortex-free and ring-shaped vortex liquids. In the repulsive regime $\kappa > 0$, our results agree quantitatively with those of magnetic quadrupolar condensates, confirming a common stabilization scenario for two-dimensional quantum fluids. More importantly, the Rydberg system distinguishes itself by offering fully isotropic, sign-switchable interactions and sustaining stable vortex droplets with winding numbers up to $m = 4$ over broad parameter ranges—features that are severely constrained in anisotropic quadrupolar counterparts.Collisions between moving zero-vorticity and vortex self-bound droplets are briefly discussed, demonstrate that their collisional dynamics are universal under the competing nonlocal repulsion and the logarithmic Lee-Huang-Yang effect.

Keywords: Bose-Einstein condensates, quantum droplets, Rydberg interactions, Lee-Huang-Yang corrections

PACS: 03.75.Hh, 67.85.-d, 67.85.De, 75.10.-b

1. Introduction

Catastrophic collapse is a well-known instability inherent to two-component Bose–Einstein condensates (BECs) under the mean-field (MF) description, which occurs as soon as the interspecies attractive scattering

*Corresponding author. E-mail: xfzhang@sust.edu.cn

overcomes the geometric mean of the intraspecies repulsive counterparts, i.e., $g_{12}^2 > g_{11}g_{22}$ [1]. This collapse phenomenon was first theoretically predicted and subsequently confirmed by a series of early ultracold-atom experiments using alkali mixtures [2,3]. A breakthrough in overcoming this intrinsic instability was made by Petrov, who introduced a beyond-mean-field stabilization mechanism rooted in the Lee–Huang–Yang (LHY) quantum fluctuation corrections, ultimately enabling the emergence of self-bound quantum droplets (QDs). Originally formulated by Lee, Huang and Yang in 1957 for hard-sphere Bose gases [4], the LHY correction was later extended to binary bosonic systems in one, two, and three dimensions (1D, 2D, and 3D), where the nonlinearity takes quadratic, logarithmic, and quartic forms, respectively [5,6]. Subsequent many-body refinements to the LHY framework have further improved the equation of state for binary bosonic mixtures [7].

In binary condensates, the scattering lengths governing both intra- and interspecies atomic collisions can be precisely adjusted via magnetically tuned Feshbach resonances, providing an efficient means to balance the mean-field nonlinearities and thereby facilitate the formation of soliton-like self-bound quantum droplets [8].In 2D configurations, the LHY correction acquires a logarithmic density dependence. Unlike its 1D and 3D counterparts, which feature quadratic attractive and quartic repulsive nonlinearities, respectively, the logarithmic LHY correction is self-adjusting, allowing self-bound droplets to emerge in both attractive and repulsive mean-field backgrounds.Recent theoretical improvements have further refined the critical stability condition for binary fluid solutions in such 2D settings [8,9].Meanwhile, systematic investigations based on density-functional theory have elucidated the properties of LHY-stabilized fundamental quantum droplets in two-dimensional geometries [10]. Moreover, several studies have reported that stable self-bound vortices with arbitrary winding numbers can be supported in binary quantum droplets [11,12], highlighting that quantum droplets provide a promising platform for studying sol itary vortex states [13].

Another type of quantum droplet has been realized in dipolar BECs, where the quartic LHY nonlinearity competes against the anisotropic attractive long-range (nonlocal) dipole-dipole interactions (DDIs) [14,15]. Follow-up studies show that stable anisotropic self-bound vortices can be supported in 2D and 3D free space [16,17]. However, while the intrinsic angular anisotropy of magnetic dipolar interactions severely limits the stability of high-order vortices, the same systems have been vigorously investigated in recent years, leading to the discovery of self-bound droplets, supersolids, and other localized structures [18–23]. Even in dipolar mixtures, where binary magnetic gases support a rich variety of miscible and immiscible droplet phases [24,25], the formation of stable vortex configurations is severely restricted by the strong anisotropy, and the creation of more complex multi-soliton or rotating hybrid states remains challenging [17]. As an alternative to dipolar settings, studies have explored vortex cluster formation and active control in cold Rydberg atomic systems with parity-time symmetric potentials [26]. Comprehensive reviews have systematically charted the development of LHY-stabilized quantum fluids in dipolar settings, summarizing both theoretical advances and experimental progress [27,28].

As an alternative route, Rydberg dressing (RD) technology has recently emerged as an all-optical strategy for engineering soft-core long-range potentials, achieved through off-resonant coupling to highly excited atomic Rydberg states [29]. The combination of RD with quantum droplets was first theoretically explored by Zhu *et al.* [30], who demonstrated the existence of three-dimensional isotropic self-bound droplets in single-component Rydberg-dressed Bose gases stabilized by the LHY correction. Multi-level RD schemes have been explored in various theoretical contexts, offering pathways for more flexible control of effective interactions [31].Despite

these advances, the full parameter space of RD interactions—particularly the roles of Rydberg strength and blockade radius—remains an active area of investigation, as recent work has focused on their influence on vortex dynamics rather than equilibrium liquid states [32].Crucially, in stark contrast to the angle-dependent dipolar or quadrupolar potentials, Rydberg interactions exhibit full spatial isotropy and permit continuous tuning of the interaction sign, which makes them a promising platform for realizing exotic quantum phases.

Numerical simulations have revealed diverse nonlinear phenomena in quantum droplets, including elongated droplets and vortices under optical Feshbach resonance [33], chiral droplet in a spin-orbit-coupled Bose gas [34], vortex-bearing quantum droplets with magnetic cores [35], and stability regimes of vortex droplets [36]. Methodologically, optimized imaginary-time propagation algorithms have been developed for high-winding-number vortex states [37,38]. The excitation properties of quantum droplets have been systematically analyzed via Bogoliubov theory and variational approaches [39,40]. In addition, studies of nonlinear excitations in two-dimensional box-trapped condensates have provided useful insights into the dynamical behavior of confined quantum fluids [41].External perturbations, including various trapping geometries, thermal effects, and rotational settings, and Rabi-coupling, etc, have been shown to modify the stability, morphology, and inter-droplet coupling of quantum droplets [42–49].

Recently, quantum droplets with magnetic quadrupole – quadrupole interactions (MQQIs) have been investigated in 2D [50]. This study exemplifies the self-adaptation effect of the logarithmic LHY correction, which competes against the long-range repulsive MQQI, allowing for the realization of stable fundamental and vortex quantum droplets. However, due to the weakly anisotropic nonlocal nature of the MQQI, stable vortex states can only be supported with a winding number up to 2; higher-order vortices are all unstable in this system. Unlike the MQQI system, the Rydberg-dressed (RD) interaction offers both attractive and repulsive nonlocal interactions through detuning tuning [51], thereby providing a broader platform for studying the self-adaptation of the logarithmic LHY correction in stabilizing 2D quantum droplets. Moreover, the RD interaction is isotropic, which facilitates the formation of stable higher-order vortex quantum droplets. Notably, the existence of 3D isotropic quantum droplets in single-component Rydberg-dressed Bose gases was recently demonstrated by Zhu et al. [30]. In that setting, the 3D LHY correction features only a quartic repulsion; hence, the RD interaction must be tuned to the attractive type. In this work, we focus on a 2D binary mixture with the logarithmic LHY correction, extending the analysis to planar vortex-bearing quantum droplets with winding numbers up to 4. The fully isotropic Rydberg soft-core potential, preserved in 2D, allows continuous tuning of the interaction from repulsive to attractive, distinguishing our system from anisotropic dipolar, quadrupolar, or 3D RD-dressed counterparts. Our results thus complement the 3D Rydberg-droplet study by establishing a versatile 2D platform for exploring both fundamental and vortex states, and by enabling direct comparison with anisotropic long-range interacting systems.

The remainder of this paper is organized as follows. Section 2 presents the theoretical model and numerical methods. Section 3 reports the stationary properties of vortex-free and vortex QDs obtained via Thomas–Fermi analysis and numerical simulations. Section 4 examines the collision dynamics of moving self-bound droplets. Section 5 summarizes the main conclusions.

2. Theoretical Model of Rydberg-Dressed Binary Condensates

This work focuses on stable QD states in quasi-2D binary BECs with optically induced RD long-range interactions. Confined by a deep transverse optical trap, the atoms move effectively in two dimensions with planar coordinate $\boldsymbol{r} = (x, y)$. The two hyperfine components are denoted by $\psi_+(\boldsymbol{r}, t)$ and $\psi_-(\boldsymbol{r}, t)$, with t the dimensionless time. Adopting the standard dimensionless formulation for RD condensates [30,49], we describe the system by the following coupled GP equations incorporating the 2D LHY quantum correction:

$$\begin{aligned} i\frac{\partial\psi_+}{\partial t} &= -\frac{1}{2}\nabla^2\psi_+ + \left(g_{11}|\psi_+|^2 + g_{12}|\psi_-|^2\right)\psi_+ \\ &\quad +\beta\psi_+\left(|\psi_+|^2 + |\psi_-|^2\right)\ln\left(|\psi_+|^2 + |\psi_-|^2\right) \\ &\quad +\kappa\psi_+\iint d\boldsymbol{r}' U_{\mathrm{RD}}(\boldsymbol{r}-\boldsymbol{r}')\left(|\psi_+(\boldsymbol{r}')|^2 + |\psi_-(\boldsymbol{r}')|^2\right), \end{aligned} \tag{1}$$

$$\begin{aligned} i\frac{\partial\psi_-}{\partial t} &= -\frac{1}{2}\nabla^2\psi_- + \left(g_{22}|\psi_-|^2 + g_{12}|\psi_+|^2\right)\psi_- \\ &\quad +\beta\psi_-\left(|\psi_-|^2 + |\psi_+|^2\right)\ln\left(|\psi_-|^2 + |\psi_+|^2\right) \\ &\quad +\kappa\psi_-\iint d\boldsymbol{r}' U_{\mathrm{RD}}(\boldsymbol{r}-\boldsymbol{r}')\left(|\psi_-(\boldsymbol{r}')|^2 + |\psi_+(\boldsymbol{r}')|^2\right). \end{aligned} \tag{2}$$

Here $\nabla^2 = \partial_x^2 + \partial_y^2$ is the planar Laplacian. The four terms on the right-hand side of Eqs. (1) and (2) account, respectively, for the kinetic energy, the contact collisions with $g_{11,22} > 0$ (intra-component repulsion) and $g_{12} < 0$ (inter-component attraction), the 2D LHY logarithmic correction weighted by β [6,7,10], and the nonlocal RD interaction governed by κ [29].

The logarithmic LHY term in Eqs. (1) and (2) is the standard quantum-fluctuation correction for a quasi-2D binary BEC near the mean-field collapse threshold [6,7,10]. It originates from short-range contact interactions. The RD interaction, on the other hand, is a long-range soft-core potential, which is included at the mean-field level through the nonlocal term.

It should be noted that, in principle, the nonlocal Rydberg interaction can modify the LHY coefficient, whose exact form requires a detailed Bogoliubov analysis. Following the results demonstrated in Ref. [30], we assume that the LHY correction acquires a modification related to the Rydberg coupling. Since this coefficient can be systematically absorbed via parameter normalization in our model, we do not calculate its explicit form in this work.

The nonlocal RD interaction is governed by the isotropic soft-core kernel

$$U_{\mathrm{RD}}(\boldsymbol{r}-\boldsymbol{r}') = \frac{1}{R_{\mathrm{c}}^6 + |\boldsymbol{r}-\boldsymbol{r}'|^6}, \tag{3}$$

which falls off as r^{-6} with interparticle separation.Here, R_{c} is the blockade radius. For convenience, R_c is scaled to 1 in the following studys. Eq. (3) stands in sharp contrast to the anisotropic MQQI potentials [50], whose angular-averaged character is purely repulsive ($\kappa > 0$), whereas the RD coupling κ can be continuously tuned across both repulsive and attractive regimes, as demonstrated in various RD studies [32].

To lower the computational cost of dual-component numerical simulations, we adopt a symmetric equal-population constraint widely used in binary QD models [7]: $\psi_+ = \psi_- \equiv \psi/\sqrt{2}$, $g_{11} = g_{22} = -g_{12} \equiv g$. Substituting symmetric constraints into Eqs. (1) and (2) simplifies the coupled system into a single scalar wave equation without losing core competing physical mechanisms:

$$i\frac{\partial}{\partial t}\psi = -\frac{1}{2}\left(\frac{\partial^2}{\partial x^2} + \frac{\partial^2}{\partial y^2}\right)\psi + \kappa\psi\int U_{\mathrm{RD}}(\boldsymbol{r}-\boldsymbol{r}')|\psi(\boldsymbol{r}')|^2 d\boldsymbol{r}' + \psi|\psi|^2\ln|\psi|^2 \tag{4}$$

In the dimensionless formulation, the LHY coefficient is absorbed as $\beta = 1$, and the density in the logarithm is normalized by $\rho_0 = 1$, i.e. $\ln(|\psi|^2/\rho_0)$.

The dynamics conserves the total particle number

$$N = \int |\psi(\boldsymbol{r})|^2 d\boldsymbol{r}, \tag{5}$$

and the system energy, which collects the kinetic, contact, LHY, and nonlocal RD parts, reads [40]

$$E = \frac{1}{2}\int \left[|\nabla\psi|^2 + |\psi|^4 \ln\left(\frac{|\psi|^2}{\sqrt{e}}\right) + \kappa \int U_{\rm RD}(\boldsymbol{r}-\boldsymbol{r}')|\psi(\boldsymbol{r}')|^2|\psi(\boldsymbol{r})|^2 d\boldsymbol{r}' \right] d\boldsymbol{r}. \tag{6}$$

All quantities in Eqs. (4)–(6) are dimensionless, with length and time scaled by 1 μm and 1 ms, respectively. Stationary solutions of Eq. (4) are sought by substituting $\psi(\boldsymbol{r},t) = \phi(\boldsymbol{r})e^{-i\lambda t}$, where λ is the chemical potential. The resulting time-independent equation is then solved numerically via imaginary-time propagation [37,38].

3. Stationary solutions for the quantum droplets

The stationary-state iteration is initiated with the trial wavefunction [13]

$$\phi^{(m)}(x,y) = Cr\exp\big(-\sigma r^2 - im\theta\big), \tag{7}$$

where the real parameters σ and C determine the spatial width and the normalization, r and θ are planar polar coordinates, and the integer m is the winding number. The case $m = 0$ yields the vortex-free ground-state QD, while $m = \pm1, \pm2, \ldots$ generates VQDs with embedded vorticity.

3.1. Fundamental quantum droplets

Figures 1(a) and 1(b) display the stationary density profiles of ground-state QDs obtained numerically for $(N,\kappa) = (1000, 0.1)$ and $(1000, 0.5)$, respectively. Their structural stability is verified by long-time propagation with weak random noise, as shown in Figs. 1(c) and 1(d). Within the $\kappa > 0$ regime, the observed flat-top density shapes follow the same variational trends as those reported for MQQI droplets [50], confirming the universal thermodynamic properties of 2D LHY-stabilized self-bound quantum fluids [6,10,50].

Since the GPE – LHY equation in Eq. (4) shares the same form as the model in Ref. [50], we can directly adopt their analytical procedure as follows. Given the flat-top density profiles of the converged ground-state solutions, we neglect the kinetic contribution and invoke the Thomas–Fermi (TF) approximation to reduce the energy functional Eq. (6) to a density-dependent form [40]:

$$E = \frac{1}{2}\left[\kappa\xi\rho^2 + \rho^2\ln\left(\frac{\rho}{\sqrt{e}}\right)\right]\Omega, \tag{8}$$

where $\rho = |\psi|^2$ is the uniform equilibrium density within the droplet, and $\Omega = N/\rho$ denotes the effective area occupied by the flat-top fluid. The constant ξ is defined as the spatial integral of the RD kernel [29]:

$$\xi \equiv \int d\boldsymbol{r}\, U_{\rm RD}(\boldsymbol{r}) = \int_0^{2\pi} d\theta \int_0^{+\infty} \frac{r dr}{1+r^6} = \frac{2\pi^2}{3\sqrt{3}}\pi^2 \approx 3.8, \tag{9}$$

with $U_{\rm RD}(\boldsymbol{r})$ given by Eq. (3). Minimization of the energy with respect to ρ, i.e., $dE/d\rho = 0$, yields closed-form analytical expressions for the equilibrium density and the corresponding effective area [40,41]:

$$\rho_e = \frac{1}{e^{1/2}e^{\kappa\xi}}, \tag{10}$$

$$\Omega_e = Ne^{1/2}e^{\kappa\xi}. \tag{11}$$

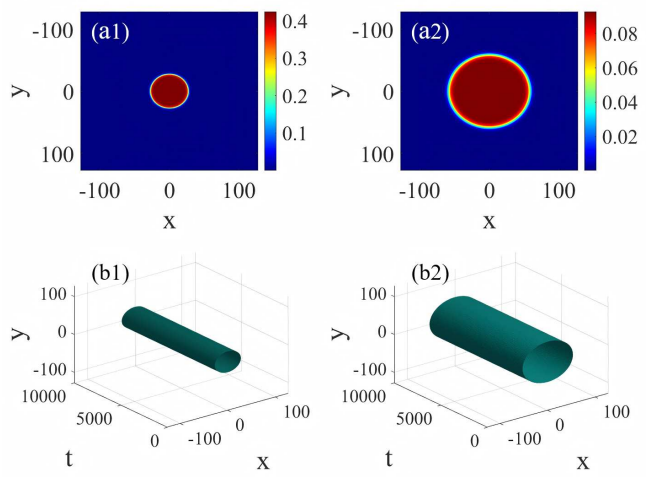


Fig. 1. Spatial density and long-time evolution snapshots of vortex-free ground QDs solved from Eq. (7). (a) Density distribution for $(N, \kappa) = (1000, 0.1)$; (b) Density distribution for $(N, \kappa) = (1000, 0.5)$; (c,d) Perturbed dynamical evolutions after adding 1% white random noise to stationary wave packets calculated from Eq. (4).

The chemical potential at equilibrium, obtained from the same energy minimum condition, takes the form

$$\lambda_e = \kappa\xi\rho_e + \rho_e \ln \rho_e. \tag{12}$$

To quantify the spatial extent of the QD wave packets, we also define the normalized effective area

$$\Omega_{\mathrm{QD}} = \frac{\left(\int |\psi|^2 d\boldsymbol{r}\right)^2}{\int |\psi|^4 d\boldsymbol{r}}. \tag{13}$$

We now turn to the dependence of three key thermodynamic quantities—the effective area Ω_{QD}, the peak density $\rho_{\max}$, and the chemical potential λ—on the particle number N and the Rydberg coupling κ. Figure 2 collects the numerical results for these observables.

Fixing $\kappa = 0.1$, we examine the N-dependence in Figs. 2(a1)–(a3). The effective area Ω_{QD} exhibits a linear growth with N (Fig. 2(a3)), a characteristic behavior of incompressible flat-top droplets that has also been reported for MQQI systems [50]. The numerical data are found to be in excellent agreement with the TF prediction, with only minor deviations [40]. For sufficiently large N, the peak density $\rho_{\max}$ reaches a plateau at approximately 0.421 (Fig. 2(a2)), reflecting the incompressibility of the self-bound superfluid phase [8]. This numerical saturation value is well reproduced by the TF estimate $\rho_e \approx 0.415$ from Eq. (10), as marked by the red dashed line in Fig. 2(a2) [41]. The chemical potential plotted in Fig. 2(a1) shows a monotonic decrease with N, i.e., $d\lambda/dN < 0$, thereby satisfying the VK stability condition [52] for self-trapped modes. At the large-N limit, the numerical λ approaches a saturation value of about -0.207, which is very close to the TF prediction $\lambda_e \approx -0.204$ [40].

We now examine the response of the system to variations in the Rydberg coupling κ while holding N fixed at 1000. The effective area Ω_{QD} increases exponentially with κ, as shown in Fig. 2(b3). The TF analytical curves are found to be nearly indistinguishable from the numerical results, with the discrepancies being primarily attributable to the omission of kinetic contributions in the TF treatment [41]. The peak density $\rho_{\max}$ and the chemical potential λ exhibit opposite trends as κ grows: $\rho_{\max}$ decreases monotonically, whereas the negative chemical potential λ increases toward zero (i.e., its magnitude decreases monotonically), as shown in Figs. 2(b2) and 2(b1). The peak density follows an exponential decrease in accordance with Eq. (10) [40]. Overall, the

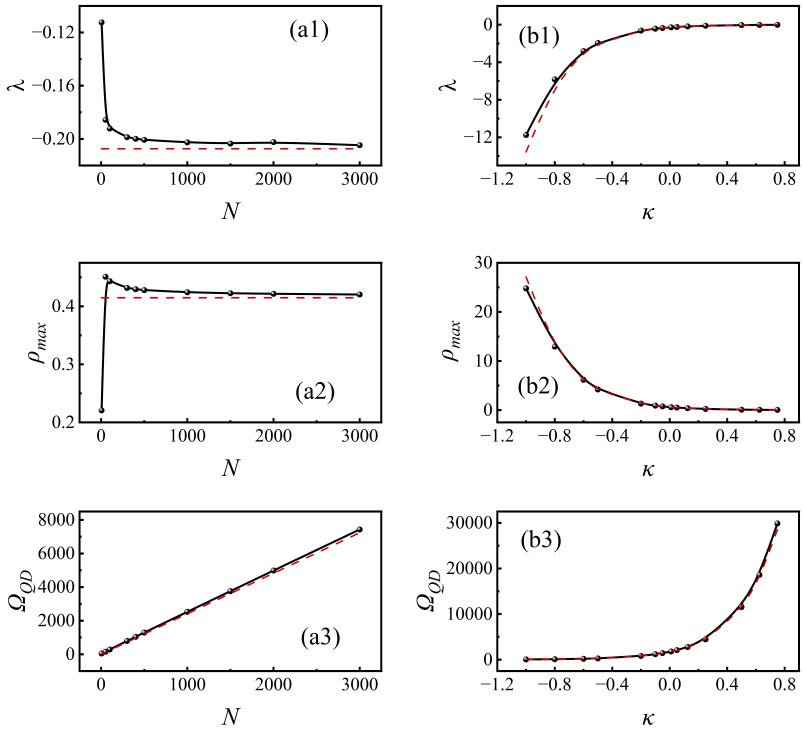


Fig. 2. Ground-state QD thermodynamics at $\kappa = 0.1$ (a1)–(a3): λ, $\rho_{\max}$, $\Omega_{\rm QD}$ vs N, and at $N = 1000$ (b1)–(b3): vs κ. Solid curves: numerical; dashed: TF predictions from Eqs. (10)–(12).

numerical data are in excellent quantitative agreement with the full set of TF predictions Eqs. (11)–(13).The sign of κ strongly affects the equilibrium. From the TF results, $\rho_e = e^{-1/2}e^{-\kappa\xi}$ and $\Omega_e = Ne^{1/2}e^{\kappa\xi}$. Thus $\kappa > 0$ expands the droplet and lowers the peak density, while $\kappa < 0$ compresses it and raises the peak density. The LHY term always provides repulsive quantum pressure, which balances the Rydberg interaction and prevents collapse. Too strong attraction (sufficiently negative κ) overcomes the LHY pressure and defines the negative stability boundary. The $\kappa > 0$ regime agrees with the MQQI case, whereas $\kappa < 0$ is unique to the Rydberg-dressed system.

3.2. quantum droplets with embedded vorticity

To generate stationary VQD solutions with different winding numbers, we feed phase-winding trial functions into the ITP routine. The resulting density and phase patterns for $m = 1$–4 at $\kappa = 0.1$ are summarized in Fig. 3, where the upper panels show the density distributions and the lower panels the phase fields. In the density subfigures, blue denotes low occupation and red marks the peak density $\rho_{\max}$; the phase contours vary across the full range $[-2\pi, 2\pi]$, reflecting the total circulation around the central phase singularity.

A notable advantage of the RD platform over its MQQI counterpart [50] is the substantially broader parameter regime over which high-m vortex structures remain stable. As the winding number increases, the central low-density core expands monotonically, while the surrounding high-density annular region moves outward and becomes progressively thinner. The phase distribution exhibits m distinct 2π branch cuts around the origin, consistent with the standard quantization condition for vortices, namely a total phase accumulation of $2\pi m$ [13]. The exact correspondence between the density-depleted core and the phase singularity provides strong evidence

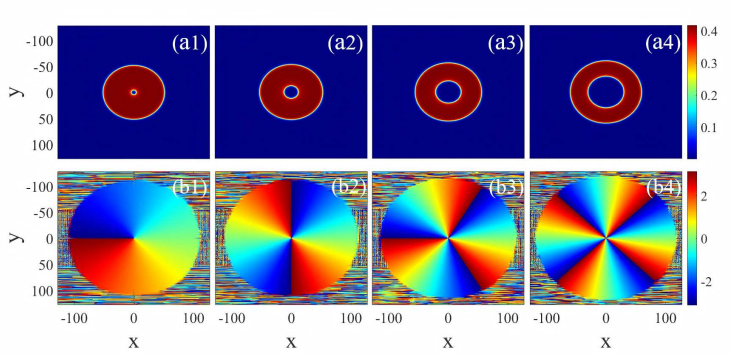


Fig. 3. Isotropic VQD solutions from Eq. (7) for $m = 1$–4 at $(N, \kappa) = (3500, 0.1)$. Upper row (a1)–(a4): density $|\psi|^2$; lower row (b1)–(b4): phase $\arg(\psi)$.

for the validity of our numerical solutions. These converged VQD wave packets will serve as initial conditions for the collision simulations discussed below, and also offer a means for identifying winding numbers through phase-sensitive experimental techniques, as demonstrated in recent experiments.

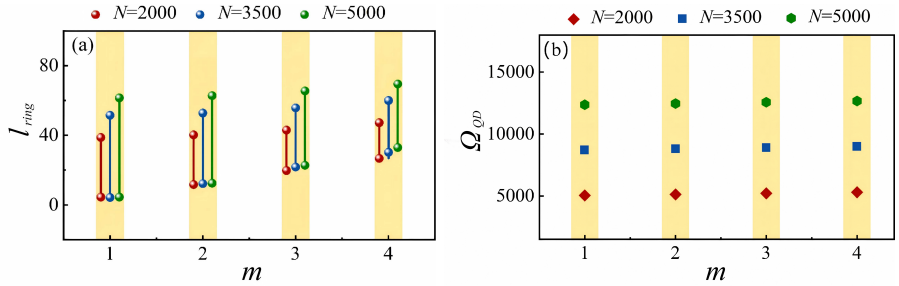


Fig. 4. Isotropic VQD geometry versus winding number m for fixed (N, κ): (a) radial width l_{ring}; (b) effective area Ω_{QD}.

As shown in Fig. 4, the radial size l_{ring} of the vortex ring grows monotonically with m. However, for a fixed total particle number N, the effective area Ω_{QD} remains nearly constant across different winding numbers. This behavior also persists in the repulsive regime of MQQI droplets [50], further confirming the incompressible nature of LHY-stabilized self-bound fluids [6,10,50]. A key distinction, however, is that while MQQI systems restrict high-m VQDs to very narrow κ intervals, the tunable RD potential supports stable ring-shaped vortex configurations over much broader ranges, including the strongly attractive coupling regime.

To quantify the geometric properties of isotropic VQDs, we extract the radial scale l_{ring} and the effective area Ω_{QD} from numerical data for various m and N. At fixed $\kappa = 0.1$, Fig. 4(a) shows that l_{ring} increases monotonically with m [13]: the core expands significantly from $m = 1$ to 3, while the growth becomes slower from $m = 3$ to 4; no complete saturation is observed. Larger N also leads to broader vortex structures, as demonstrated by the $N = 5000$ curve lying above those for $N = 3500$ and 2000. In contrast, Ω_{QD} remains nearly constant for a given N across different m (Fig. 4(b)), with values around 5000, 9000, and 12000 for $N = 2000$, 3500, and 5000, respectively. Thus, N governs the overall spatial extent of the droplet, while m only rearranges the internal density distribution (core and ring) without changing the total area. The effective area formula Eq. (13) captures this global coverage [40]; although vortices introduce a low-density core, the outer annulus retains a flat-top profile, preserving the incompressible character of the fluid [6,10]. Phase-sensitive

imaging is required to detect the vortex core, whereas the overall size directly reflects the atom number.

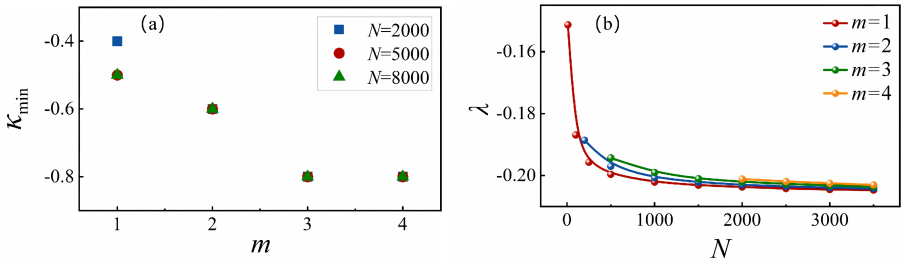


Fig. 5. (a) Stability threshold $\kappa_{\min}$ for VQDs with $m = 1$ to 4 at different N. The threshold shifts to more negative values with increasing m and is essentially independent of N. (b) Chemical potential λ vs N for VQDs with $m = 1$ to 4 at $\kappa = 0.1$. All branches satisfy $d\lambda/dN < 0$; they are separated by m for $N < 500$ and merge to about -0.205 for $N > 2000$.

The stability of isotropic VQDs is governed by a balance between the attractive RD interaction and the extra kinetic energy arising from phase gradients around the vortex. Figure 5(a) presents the threshold coupling $\kappa_{\min}$ for different winding numbers: the boundary moves to more negative values with increasing m, taking $\kappa_{\min} \approx -0.4$ for $m = 1$, -0.6 for $m = 2$, and about -0.8 for both $m = 3$ and 4. Curves for $N = 2000$, 5000, and 8000 overlap nearly perfectly, indicating that the stability threshold is essentially insensitive to the atom number and is determined primarily by m. This behavior contrasts sharply with MQQI systems, where high-order vortices are confined to narrow positive-κ windows [50]. It is worth emphasizing that the key factor is the isotropic symmetry, not the soft-core structure. Ref. [50] also has a soft-core potential, but its lack of strict axisymmetry causes vortex-axis splitting and dynamical deformations. In contrast, our strict axisymmetry pins the vortex axes at the center without splitting, ensuring excellent stability. Larger m creates steeper phase gradients around the core, requiring stronger RD attraction to compensate the elevated kinetic energy and prevent centrifugal expansion. The threshold drops most rapidly from $m = 1$ to 3 and then levels off, suggesting that beyond a certain winding number the soft core can accommodate additional circulation without further increasing the energy cost.

Figure 5(b) shows the λ-N curves for VQDs with $m = 1$–4 at fixed $\kappa = 0.1$. Crucially, larger m gives rise to stronger azimuthal instability, requiring a larger N to sustain the vortex—this is manifested in the λ-N curves by the fact that branches with higher m appear only at progressively larger N: the $m = 1$ branch emerges near $N \approx 200$, while $m = 3$ and 4 require $N \approx 500$ to appear. In other words, for each m there exists an N threshold below which the VQD cannot exist, and this threshold increases with m. This threshold behavior is unique to vortex states—the ground state ($m = 0$) has no such N threshold and exists at arbitrarily small N. All branches display a decreasing trend with increasing N, eventually approaching saturation. In the low-N regime ($N < 500$), the curves are clearly separated by m: the $m = 1$ branch exhibits the highest λ (about -0.15), followed by $m = 2$, while the $m = 3$ and $m = 4$ branches nearly coincide near -0.19. For $N > 2000$, the four curves gradually merge and converge to a common saturated value around -0.205, indicating that the winding number becomes essentially irrelevant in the large-N limit. Importantly, all branches satisfy $d\lambda/dN < 0$, meeting the VK stability criterion [52] for self-trapped localized modes. A vortex carries extra kinetic energy. For $\kappa > 0$, the repulsive nonlocal interaction competes with this kinetic pressure. For $\kappa < 0$, the attractive interaction can compensate it and support stable vortices. Hence $\kappa_{\min}$ shifts to more negative values as m increases, as shown in Fig. 5(a). This differs from MQQI systems, where the purely repulsive interaction

restricts stable vortices to $m \leq 2$ over narrow windows. The sign-tunable Rydberg interaction therefore provides a much broader parameter space, especially for $\kappa < 0$. Near the stability threshold, real-time propagation shows that the dominant instability is radial collapse. When κ is more negative than $\kappa_{\min}$, the ring contracts inward, the peak density increases rapidly, and the droplet collapses. No pronounced azimuthal splitting is observed.

It should be noted that while traditional nonlinear self-localized systems typically suffer from azimuthal instability at higher winding numbers, quantum droplets can suppress this due to the competition between the mean-field and LHY corrections. Furthermore, unlike non-axisymmetric systems where vortex axes may split, the isotropic symmetry here keeps the vortex axis pinned at the center without deformation. A larger particle number is required to stabilize higher-m vortices, as shown in Fig. 5(b).

4. Dynamics of the quantum droplets

We now investigate the dynamical behavior of the self-bound droplets, which is essential for understanding their nonlinear interaction properties and topological robustness [33]. It has been established that velocity kicks can set QDs into motion in binary BECs, enabling head-on collision studies. In the present RD system, we prepare two well-separated QD wave packets propagating in opposite directions along x and simulate their collisions, examining how the impact velocity, the RD coupling κ, and the winding number m influence the final outcomes.

The initial configuration for a head-on collision takes the form

$$\psi(x, y, t = 0) = \phi(x - d_0, y)e^{-iv_0 x} + \phi(x + d_0, y)e^{iv_0 x}, \tag{14}$$

where $\phi(x \pm d_0, y)$ denotes the stationary profile of a QD or VQD initially centered at $x = \mp d_0$, with the separation d_0 (128 or 64) chosen to avoid any initial overlap. The parameter v_0 controls the collision speed, and the phase factors $e^{\pm iv_0 x}$ impart opposite momenta to the two droplets.

4.1. Collisions between fundamental quantum droplets

The numerical integration of the time-dependent GPE–LHY equation is performed using the split-step Fourier method. During the collision process, we monitor the evolution of the density profile, the angular momentum $\bar{\mathcal{L}}_z$, and the total energy to characterize the mode transformation and assess the structural integrity of the droplets. We begin by examining head-on collisions of travelling ground-state QDs ($m = 0$).

Previous studies have investigated a variety of dynamical processes in quantum droplets, ranging from inelastic collisions in binary contact-interacting mixtures to the formation of metastable patterns in dipolar settings [53,54]. Collisions of symmetric two-component droplets with balanced intraspecies scattering lengths have also been explored, as have the scattering properties of moving anisotropic vortex QDs in two dimensions, where vortex–antivortex–vortex bound states can be generated [17].

The collision outcomes for ground-state QDs are summarized in Fig. 6 for the parameter set $(N, d_0, \kappa) = (1000, 128, 0.01)$. At low kick velocity ($v_0 = 0.1$, panels (a1)–(a6)), the two droplets merge into a single breather exhibiting periodic oscillations, consistent with previously reported behavior of self-bound droplets [55]. Increasing the kick to $v_0 = 0.12$ (panels (b1)–(b6)) drives the system into the quasi-elastic regime, where the

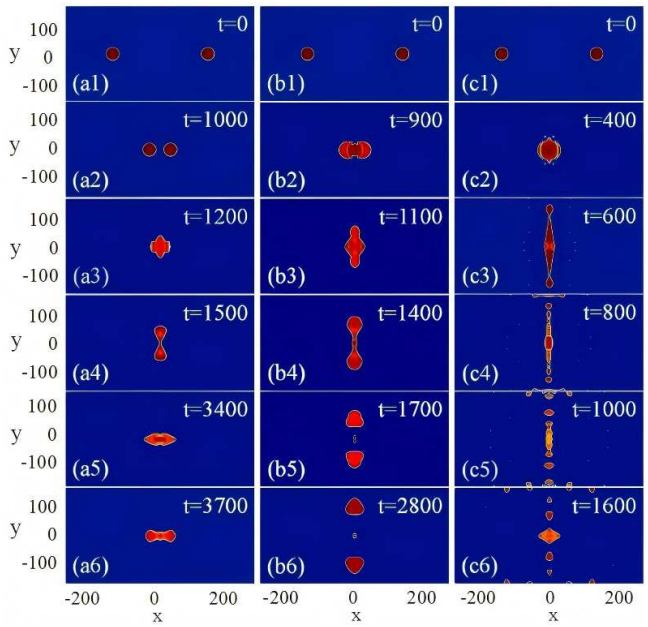


Fig. 6. Collision dynamics of isotropic ground-state QDs from Eq. (14) with $d_0 = 128$, $(N, \kappa) = (1000, 0.01)$. (a1)–(a6) Inelastic fusion at $v_0 = 0.1$; (b1)–(b6) 90° quasi-elastic deflection at $v_0 = 0.12$; (c1)–(c6) fragmentation at $v_0 = 0.3$.

droplets separate and are deflected by 90° [56]. At high velocity ($v_0 = 0.3$, panels (c1)–(c6)), the collision becomes strongly inelastic and fragments the droplets into multiple pieces.

These three regimes–fusion, 90° deflection, and fragmentation–are qualitatively similar to those observed in MQQI droplets for $\kappa > 0$ [50], confirming the universal nature of LHY-stabilized 2D fluids [6,10,50]. However, unlike the MQQI case where such behaviors are confined to narrow parameter ranges, the RD system exhibits these collision regimes over a much broader region of the parameter space, benefiting from the continuously tunable and isotropic nature of the Rydberg potential. The critical velocities for regime transitions are also influenced by N and κ, as both parameters affect the droplet size, but the wider stability windows of the RD platform make it a more flexible setting for exploring collision dynamics.

4.2. Collision between moving vortex quantum droplets

We now turn to the collision dynamics of vortex-bearing droplets. Figure 7 displays the results for VQDs with $m = 1$ under the initial configuration Eq. (14), with parameters $(N, d_0, \kappa) = (1000, 128, 0.01)$. To characterize the vorticity of the colliding droplets, we compute the averaged angular momentum

$$\bar{\mathcal{L}}_z = \frac{1}{N} \int \phi^* \hat{\mathcal{L}}_z \phi \, d\boldsymbol{r}. \tag{15}$$

At low impact velocity ($v_0 = 0.01$, Figs. 7(a1)–(a6)), the two VQDs undergo a contactless collision: they rebound and preserve their initial winding numbers. The angular momentum for each outgoing droplet is found to be $\bar{\mathcal{L}}_z \approx 1$, indicating that the vorticity is fully retained during the process. This rebounding behavior is absent in collisions of vortex-free droplets, highlighting the distinct dynamical response of topological states.

At intermediate velocities ($v_0 = 0.03$), the two VQDs coalesce and subsequently break apart into several pieces without discernible vorticity, suggesting the transient formation of a vortex breather [36]. For a slightly higher kick ($v_0 = 0.04$), the collision becomes inelastic and produces a long-lived vortex breather (Figs. 7(c1)–

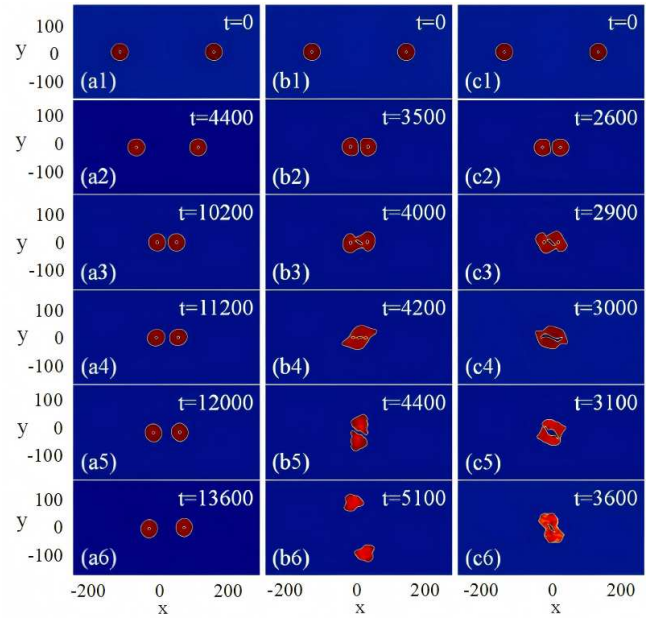


Fig. 7. Head-on collisions of VQDs with $m = 1$ for $(N, \kappa) = (1000, 0.01)$. (a1)–(a6) contactless rebound ($v_0 = 0.01$); (b1)–(b6) fragmentation ($v_0 = 0.03$); (c1)–(c6) vortex breather formation ($v_0 = 0.04$).

(c6)). The angular momentum of this breather is found to be $\bar{\mathcal{L}}_z \approx 1.983$, close to the value 2 expected for a doubly quantized vortex state, indicating that angular momentum is nearly conserved during the collision process [13]. This observation confirms the existence of stable VQDs with $m = 2$ in the present system.

These collision behaviors of VQDs are qualitatively similar to those observed in MQQI systems [50], further confirming that the collisional dynamics of binary quantum droplets—both for fundamental and vortex states—exhibit universal features independent of the specific form of the long-range interaction [50]. While the universal collision scenarios are reproduced in both systems, the RD platform offers a decisive advantage: the coupling strength κ is continuously tunable across both repulsive and attractive regimes, allowing access to a much broader parameter space for exploring vortex droplet collisions, in contrast to the purely repulsive and narrow-range MQQI case.

5. Conclusion

We have systematically investigated two-dimensional fundamental and vortex quantum droplets in a binary BEC with Rydberg soft-core interactions, modeled by the GP equation incorporating the 2D LHY logarithmic correction and a tunable isotropic nonlocal potential. By means of imaginary-time propagation and real-time evolution, we have obtained stable self-bound droplets for both zero-vorticity and vortex-carrying states with winding numbers up to $m = 4$. For fundamental droplets, the TF approximation provides accurate analytical predictions for the effective area, peak density, and chemical potential that agree quantitatively with numerical simulations. For vortex droplets, stable solutions with $m = 1$ to 4 are obtained over broad parameter ranges enabled by the fully isotropic Rydberg potential, and we have systematically studied their density profiles, phase structures, and stability properties. The stability threshold $\kappa_{\min}$ shifts to more negative values with increasing m and is essentially independent of N, confirming that the RD coupling rather than the particle population is the primary factor controlling VQD stability. More importantly, larger m gives rise to stronger azimuthal instability,

requiring a larger N to sustain the vortex—this is manifested by the fact that branches with higher m emerge only at progressively larger N, and for each m there exists an N threshold below which the VQD cannot exist, a behavior unique to vortex states as the ground state has no such threshold. All branches satisfy $d\lambda/dN < 0$, meeting the VK stability criterion. Collision dynamics reveal three generic regimes—inelastic fusion at low velocities, quasi-elastic 90° deflection at intermediate velocities, and fragmentation at high velocities—with vortex droplets additionally exhibiting a contactless rebound at small collision speeds.

More importantly, the RD platform offers several decisive advantages over its quadrupolar counterpart. The Rydberg-mediated potential is fully isotropic, in contrast to the inherent angular dependence of quadrupolar. The coupling strength κ can be continuously tuned across both repulsive and attractive domains, providing access to the negative-κ regime that remains largely unexplored, whereas MQQI systems are restricted to purely repulsive interactions; combined with the logarithmic LHY correction, this allows continuous control of the equilibrium density and the vortex stability threshold. Furthermore, vortex droplets with winding numbers up to $m = 4$ remain stable over broad parameter intervals, in sharp contrast to the extremely narrow stability windows typical of quadrupolar systems. These features establish the Rydberg-dressed BEC as a versatile and highly controllable platform for studying the self-adaptation of the logarithmic LHY correction in stabilizing two-dimensional quantum fluids. Our results also confirm the universal properties of quantum droplets stabilized by the 2D LHY effect under competing nonlocal interactions. Several promising directions remain for future investigation, including extending the present symmetric configuration ($\psi_1 = \psi_2$, $m_1 = m_2$) to asymmetric cases with unequal particle numbers and different winding numbers in the two components to support exotic states such as mixed vortices and hidden vortices [57–59], exploring whether the inclusion of LHY correction can give rise to novel supersolid phases as proposed by Zhang et al. [60], systematically studying the attractive regime $\kappa < 0$, and extending the analysis to full three-dimensional geometries. Together with other theoretical and experimental investigations on self-bound quantum droplets [61,62], these extensions would further enrich the understanding of LHY-stabilized quantum fluids in Rydberg-dressed configurations.

Acknowledgment

This work was supported by the National Natural Science Foundation of China under Grants No. 12175129, No. 12475004, No. 12175027, and No. 12005125; by the Key Research Program of Frontier Sciences of Chinese Academy of Sciences under Grant No. ZDBS-LY7016; by the Shaanxi Fundamental Science Research Project for Mathematics and Physics under Grant No. 22JSY034, No. 25JSQ017, and the Natural Science Basic Research Program of Shaanxi Province under Grant No. 2026JC-JCQN-006; by the Key Research and Development Projects of Shaanxi Province under Grant No. 2024GX-YBXM-564; by the Scientific Research Program Funded by Shaanxi Provincial Education Department under Program No. 23JP020; and by The Youth Innovation Team of Shaanxi Universities.

References

[1] Petrov D S 2015 *Phys. Rev. Lett.* **115** 155302

[2] Cabrera C R, Tanzi L, Sanz J, Naylor B, Thomas P, Cheiney P and Tarruell L 2018 *Science* **359** 301

[3] Cheiney P, Cabrera C R, Sanz J, Naylor B, Tanzi L and Tarruell L 2018 *Phys. Rev. Lett.* **120** 135301
[4] Lee T D, Huang K and Yang C N 1957 *Phys. Rev.* **106** 1135
[5] Ota M and Astrakharchik G E 2020 *SciPost Phys.* **9** 020
[6] Petrov D S and Astrakharchik G E 2016 *Phys. Rev. Lett.* **117** 100401
[7] Guo Z, Jia F and Li L 2021 *Phys. Rev. Res.* **3** 033247
[8] d'Errico C, Zaccanti M, Fattori M, Roati G, Inguscio M, Modugno G and Simoni A 2007 *New J. Phys.* **9** 223
[9] Spada G, Pilati S and Giorgini S 2023 *Phys. Rev. Lett.* **131** 173404
[10] Zhang F and Yin L 2025 *Chin. Phys. Lett.* **42** 010302
[11] Li Y, Chen Z, Luo Z, Huang C, Tan H, Pang W and Malomed B A 2018 *Phys. Rev. A* **98** 063602
[12] Lin Z, Xu X, Chen Z, Yan Z, Mai Z and Liu B 2021 *Commun. Nonlinear Sci. Numer. Simul.* **93** 105536
[13] Chen G H, Wang H C, Deng H M and Malomed B A 2024 *Chin. Phys. Lett.* **41** 020501
[14] Schmitt M, Wenzel M, B?ttcher F, Ferrier-Barbut I and Pfau T 2016 *Nature* **539** 259
[15] Zhang F and Yin L 2022 *Chin. Phys. Lett.* **39** 060301
[16] Li G, Zhao Z, Zhang R, Chen Z, Liu B, Malomed B A and Li Y 2024 *Front. Phys.* **19** 22202
[17] Li G, Zhao Z, Zhang R, Chen Z, Liu B, Malomed B A and Li Y 2024 *Phys. Rev. Lett.* **133** 053804
[18] Edmonds M, Bland T and Parker N 2020 *J. Phys. Commun.* **4** 125008
[19] Chomaz L, Ferrier-Barbut I, Ferlaino F, Laburthe-Tolra B, Lev B L and Pfau T 2022 *Rep. Prog. Phys.* **86** 026401
[20] Norcia M A, Politi C, Klaus L, Poli E, Sohmen M, Mark M J, Bisset R N, Santos L and Ferlaino F 2021 *Nature* **596** 357
[21] Bland T, Poli E, Politi C, Klaus L, Norcia M A, Ferlaino F, Santos L and Bisset R N 2022 *Phys. Rev. Lett.* **128** 195302
[22] Pal S, Baillie D and Blakie P B 2022 *Phys. Rev. A* **105** 023308
[23] Schmidt M, Lassabli猫re L, Qu茅m茅ner G and Langen T 2022 *Phys. Rev. Res.* **4** 013235
[24] Bisset R N, Ilg T, ?imjanovski L and Santos L 2021 *Phys. Rev. Lett.* **126** 025301
[25] Smith J C, Baillie D and Blakie P B 2021 *Phys. Rev. Lett.* **126** 025302
[26] Fan Z, Shi Y, Wang H, Zhao Y, Peng W and Xu S 2024 *Chin. Phys. B* **33** 120306
[27] Malomed B A 2021 *Front. Phys.* **16** 22504
[28] Guo M Y and Pfau T 2021 *Front. Phys.* **16** 32202
[29] Zhang Y C, Hang C, Malomed B A and Huang G X 2025 *Phys. Rev. E* **111** 024205
[30] Zhu H, Ma Y Q, Bai W K, Yu Y M, Ye F F, Li Y Y, Zhuang L and Liu W M 2024 *Phys. Rev. Res.* **6** 023151
[31] Chen X W, Zhao Z B, Zheng X T, Huang H, Wang H C, Liu Y and Chen G H 2024 *Phys. Lett. A* **517** 129654
[32] Zhong Y, Yang D F, Liu Y X, Li J, Triki H and Zhou Q 2025 *Chin. Phys. Lett.* **42** 080002
[33] Li G, Zhao Z, Zhang R, Chen Z, Liu B, Malomed B A and Li Y 2025 *Phys. Rev. A* **112** 013318
[34] Luo T and Cui X 2025 *Phys. Rev. A* **112** 043312

[35] Li S and Saito H 2024 *Phys. Rev. Res.* **6** L042049

[36] Salgueiro J R, Paredes A, Guerra-Carmenate J and Michinel H 2024 *Results Phys.* **64** 107923

[37] Chiofalo M L, Succi S and Tosi M P 2000 *Phys. Rev. E* **62** 7438

[38] Yang J and Lakoba T I 2008 *Stud. Appl. Math.* **120** 265

[39] Banerjee A and Majumder D 2024 *Ann. Phys.* **470** 169810

[40] Paredes A, Salgueiro J R and Michinel H 2024 *Chaos Solitons Fractals* **186** 115297

[41] Niu Z M and Gao R 2024 *Chin. Phys. B* **33** 020314

[42] Gu Q and Cui X 2023 *Phys. Rev. A* **108** 063302

[43] Wang J, Liu X J and Hu H 2021 *Chin. Phys. B* **30** 010306

[44] Zhou Z, Chen T, Zhu B and Zhong H 2025 *Chaos Solitons Fractals* **199** 116700

[45] Poparić I, Marković L V and Boronat J 2025 *Phys. Rev. A* **112** 053317

[46] Nikolaou S, Kavoulakis G M and Ögren M 2024 *Phys. Rev. A* **110** 043302

[47] Nikolaou S, Kavoulakis G M and Ögren M 2024 *Phys. Rev. A* **109** 043304

[48] Lavoine L, Hammond A, Recati A, Petrov D S and Bourdel T 2021 *Phys. Rev. Lett.* **127** 203402

[49] Hsueh C H, Wang C W and Wu W C 2020 *Phys. Rev. A* **102** 063307

[50] Yang A, Zhou J, Liang X, Li G, Liu B, Luo H B, Malomed B A and Li Y 2024 *New J. Phys.* **26** 053037

[51] Glaetzle A W, Nath R, Zhao B, Pupillo B and Zoller P 2012 *Phys. Rev. A* **86** 043403

[52] Vakhitov N G and Kolokolov A A 1973 *Radiophys. Quantum Electron.* **16** 783

[53] Böttcher F, Schmidt J N, Wenzel M, Hertkorn J, Guo M, Langen T and Pfau T 2021 *Rep. Prog. Phys.* **84** 012403

[54] Zhang Y C and Pohl T 2024 *Phys. Rev. Res.* **6** 023023

[55] Lavoine T and Bourdel T 2021 *Phys. Rev. A* **103** 033312

[56] Zhang Z, Nie Y H, Zheng J H and Yang T 2023 *AIP Adv.* **13** 055130

[57] Brtka M, Gammal A and Malomed B A 2010 *Phys. Rev. A* **82** 053610

[58] Chen Y X, Cai X Y, Liu B, Jiang X D and Li Y Y 2022 *Acta Phys. Sin.* **71** 200302

[59] Huang H, Wang H C, Chen M N, Lim C S and Wong K C 2022 *Chaos Solitons Fractals* **158** 112079

[60] Han W, Zhang X F, Wang D S, Jiang H F, Zhang W and Zhang S G 2018 *Phys. Rev. Lett.* **121** 030404

[61] Semeghini G, Ferioli G, Masi L, Mazzinghi C, Wolswijk L, Minardi F, Modugno M, Modugno G, Inguscio M and Fattori M 2018 *Phys. Rev. Lett.* **120** 235301

[62] Dong L and Kartashov Y V 2021 *Phys. Rev. Lett.* **126** 244101 .